An Adaptive Snake Model for Ultrasound Image Segmentation: Modified Trimmed Mean Filter, Ramp Integration and Adaptive Weighting Parameters

Chung-Ming Chen and Henry Horng-Shing Lu

Ultrason Imaging 2000 22: 214
DOI: 10.1177/016173460002200403

ULTRASONIC IMAGING 22, 214-236 (2000)

An Adaptive Snake Model for Ultrasound Image Segmentation: Modified Trimmed Mean Filter, Ramp Integration and Adaptive Weighting Parameters

CHUNG-MING CHEN[1] AND HENRY HORNG-SHING LU[2]

[1]*Institute of Biomedical Engineering*
National Taiwan University
Taipei, Taiwan
Email: chung@lotus.mc.ntu.edu.tw

[2]*Institute of Statistics*
National Chiao-Tung University
Hsn-Chu, Taiwan

The snake model is a widely-used approach to finding the boundary of the object of interest in an ultrasound image. However, due to the speckles, the weak edges and the tissue-related textures in an ultrasound image, conventional snake models usually cannot obtain the desired boundary satisfactorily. In this paper, we propose a new adaptive snake model for ultrasound image segmentation. The proposed snake model is composed of three major techniques, namely, the modified trimmed mean (MTM) filtering, ramp integration and adaptive weighting parameters. With the advantages of the mean and median filters, the MTM filter is employed to alleviate the speckle interference in the segmentation process. The weak edge enhancement by ramp integration attempts to capture the slowly varying edges, which are hard to capture by conventional snake models. The adaptive weighting parameter allows weighting of each energy term to change adaptively during the deformation process. The proposed snake model has been verified on the phantom and clinical ultrasound images. The experimental results showed that the proposed snake model achieves a reasonable performance with an initial contour placed 10 to 20 pixels away from the desired boundary. The mean minimal distances from the derived boundary to the desired boundary have been shown to be less than 3.5 (for $CNR \geq 0.5$) and 2.5 pixels, respectively, for the phantom and ultrasound images.

KEY WORDS: Adaptive weighting parameters; modified trimmed mean filter; ramp integration; snake model; ultrasound image segmentation.

1. INTRODUCTION

Ultrasonic imaging has become a widely-used imaging modality due to its noninvasiveness, real-time scanning, low-cost and versatility. While new applications of ultrasonic imaging are still being discovered, it has been applied to many areas in medicine ranging from the OB/GYN to neurosurgery. It provides not only a real-time anatomical view into soft tissues, but also such functional information as blood flow speed and tissue elasticity. Versatile as it is, a further analysis, especially an automatic or semi-automatic quantitative analysis, of an ultrasound image has been considered difficult compared to many other imaging modalities, such as MRI and CT. The major difficulty in analyzing an ultrasound image arises from its intrinsic textural pattern formed by the speckle and tissue-related textures composed of quasirepetitive patterns or sporadic spots. Although both the speckle and tissue-related textures play an important role in many clinical applications, e.g., diagnosis of liver cirrhosis,[1] they have been generally regarded as noise from the viewpoint of image segmentation using nontextural approaches. Even for textural image segmentation techniques, their performances are often seriously degraded since the noise may not be eliminated thoroughly due to the quasiregular nature of the tissue-related textures. A typical example is

0161-7346/00 $18.00

when one attempts to segment a tumor from an ultrasound image automatically, the classic segmentation techniques frequently fail to identify the boundary of the object of interest effectively because of these noises.

Conventionally, quantitative analysis usually requires human intervention to specify the region-of-interest (ROI) to be measured. For instance, to measure the size of a tumor, a medical staff would need to make several marks so that the computer can calculate the diameters of the tumors according to the marks. However, the manual approaches suffer from at least two problems. One is that the diagnostic results are not only operator-dependent but also time-dependent. In other words, different medical staffs may give different analysis results and even the same person may make a different measurement for an ROI at a different time. This is potentially a very serious problem since it may affect the decision of treatment planning. The other problem is that it may take a great amount of time for a medical staff to accomplish the task. For example, for a 3D object composed of hundreds of 2D slices, it may take more than half an hour for an experienced staff to manually draw the boundaries of the objects of interest in all slices.

Among the various types of quantitative analyses, segmentation is one of the major analysis tasks performed by medical staffs. To avoid the two problems inherently in the manual approaches, extensive studies on automatic and semi-automatic segmentation of the ultrasound images have been made in the past. As examples, automated segmentation of ultrasound images have been attempted for such objects as fetal femurs,[2] lower legs,[3] lumen-intima and media-adventitia of intracoronary images,[4,5] ovarian cysts[6] and prostates.[7] Although many previous investigators have achieved satisfactory results for some specific problems, their approaches are basically application-dependent and may not be effectively applied to segment other types of ultrasound images.

In contrast to the application-specific segmentation approaches, an ideal general segmentation approach is expected to be able to segment out various types of objects of interest, e.g., fetal femurs, cysts, tumors and prostates. However, general ultrasound image segmentation is far more difficult than application-specific segmentation since not much prior information may be utilized in the design of the segmentation algorithms. Due to the complex nature of an ultrasound image, a general segmentation approach may need to find out the ill-defined object boundary, which consists of two essential tasks, i.e., determining the ill-defined edges and providing a closed contour for the underlying object of interest. To achieve this goal, recently, the snake model has received a great attention as a general technique for ultrasound image segmentation.[8,-13]

The snake model was first proposed by Kass et al,[14] who suggested a contour deformation mechanism guided by an energy minimization process. The energy function of a snake model is usually composed of energy terms describing the internal force of the snake, an image force from the image and an external force like constraints. Although the snake model promises a closed boundary once it converges to a local minimum, the intrinsic noise of an ultrasound image has made a snake easily trapped in an undesired local minimum. As a result, the conventional snake model is compelled to have the initial contour very close to the desired boundary, which has made the snake model impractical for clinical use. To cope with the intrinsic noise and to augment the penetrating capability of the snake, we propose a new snake model in this paper with three important features, namely, a modified-trim-mean-filter (MTMF), adaptive weighting parameters and weak-edge enhancement by integration. The MTMF filter provides a fast and reasonably good performance on speckle reduction, as demonstrated by Loupas et al.[15] The adaptive weighting parameter allows the weighting of each energy term to change adaptively during the deformation process. The weak edge enhancement by integration attempts to capture the slowly-varying edges, which are hard to capture by conventional snake models.

This paper is organized as follows. The methods and materials employed in this study are described in section 2. It contains the proposed snake model as well as generation and acquirement of the images used for performance evaluation, which includes phantom images with simulated speckles and clinical ultrasound images. Experimental results and discussions are provided in section 3. Conclusions are given in section 5.

2. METHODS AND MATERIALS

The basic idea of the snake model is to guide contour deformation by minimizing an energy function, usually composed of an internal force, image force and external force. While various kinds of energy have been proposed in the past, a general energy function may be written as

$$E_{snake}(\Gamma(s)) = \oint_{\Gamma} [E_{int}(\upsilon(s)) + E_{image}(\upsilon(s)) + E_{external}(\upsilon(s))]ds \tag{1}$$

where $\Gamma(s) = (x(s), y(s))$ is the parametric representation of the contour. In Kass' work, E_{int} denotes the internal energy of the spline due to bending, which may be defined as ,

$$E_{\text{int}} = \left(\alpha(s)|v_s(s)|^2 + \beta(s)|v_{ss}(s)|^2\right)/2 \tag{2}$$

The first-order and the second-order terms, i.e., $v_s(s)$ and $v_{ss}(s)$, make the snake behave like a membrane and thin plate, respectively. One may also regard the first- and second-order terms as a measurement of the continuity and curvature of the snake. The internal force imposes a smoothness constraint on the snake. The image energy, E_{image}, accounts for the guidance force from the image, which attempts to push the snake toward the salient features of the image. One typical image force is the edge strength of the image. The external energy, $E_{external}$, is to take into account other possible forces, which may help the snake deform toward the desired boundary. For example, one may impose a shape constraint on the snake to regularize the snake deformation.[16]

Given an energy function, the energy minimization mechanism plays an important role in guiding the snake to find the desired boundary. At least three types of energy minimization mechanisms have been employed previously. One method attempts to find the minimum energy point by using mathematical optimization techniques; e.g., Kass et al employed the variation of calculus to find the iterative relations, which suggests the next position to move to for each snake element, called a *snaxel*. Based on the concept of the greedy algorithm, another method moves each snaxel to the next lower energy state by searching a finite neighborhood of each snaxel.[17] The third approach uses optimization techniques such as dynamic programming[16] and simulated annealing,[18] trying to find the global minimum of the given energy function.

The salient feature of the snake model is that it provides an elegant energy-guided methodology to attain a continuous contour for the object of interest. For an image with a high signal-to-noise (S/N) ratio and a well-defined boundary, the snake model indeed has demonstrated its great capability in finding the desired boundary in varieties of applications.[14-19] However, if the S/N ratio is low, the snake may be easily trapped in the local minimum formed by the noise. If a significant portion of the desired boundary is either missing or has a weak edge strength, the snake may not be able to be latched at the preferred location. Although a better

energy minimization mechanism may partially alleviate this dilemma, the very fundamental problem is that the global minimum may not occur at the desired boundary due to the noise, the weak edges and some other intrinsic properties of the snake model. As a result, most of the conventional snake models require the initial contour to be very close to the desired boundary to reduce the possibility of being trapped by the undesired local minimum.

To overcome the interference of the noise and to catch the weak edges, i.e., the slowly-varying edges, an adaptive snake model is proposed in this paper for ultrasound image segmentation. The idea is to highlight the weak edges by an integration type of edge detector and to adjust the weighting factors of the energy terms adaptively to augment the capability of penetrating noises for the snake to allow a distant initial contour. The proposed snake model is presented in detail below, followed by the description of the phantom images and clinical ultrasound images used in the performance analysis.

2.1 Adaptive snake model

The proposed snake model is composed of three major schemes, namely, the MTM filter, ramp integration and adaptive weighting. The MTM filter is responsible for reducing the speckle and tissue-related texture to a great extent in a short time. The ramp integration not only can enhance the weak edges but also can further suppress the interference of the residual noises. The adaptive weighting scheme takes into account the importance of difference energy terms at different deformation stages, attempting to attain a better noise-penetrating capability for the snake. As an overview, the proposed snake model is illustrated in figure 1.

Contour initialization and snaxel sampling

The initial contour of the snake is a closed contour enclosing the object of interest. It can be a polygon or a regular shape like a rectangle or an ellipse. Once the initial contour is generated, two classes of snake deformation may be found in the previous snake models. One is *continuous*,[14] i.e., the snake energy is computed over the entire snake. The other is *discrete*,[17] i.e., the snake energy is calculated only for a discrete set of points in the snake, called *snaxels*. While the continuous approaches promise a better estimation of the internal energy of a snake, the discrete approaches tend to be more computationally efficient. Aiming at a computationally efficient methodology, the proposed snake model adopts the discrete approach. Initially, N snaxels are selected from the initial snake and the number of points on the snake between every two adjacent snaxels is a constant, denoted as d.

Snaxel movement

Let p_i and V_i denote the i^{th} snaxel and the position of the i^{th} snaxel, respectively. The snaxel movement is based on a greedy search, i.e., at each step, each snaxel V_i seeks for the position with the lowest energy state within the searching window to move to. As depicted in figure 2, the searching window is a window of l pixels long in the searching direction and w pixels wide in the direction perpendicular to the searching direction. Let $\vec{u}_i = \vec{V}_i - \vec{V}_{i-1}$. Then, the searching direction is defined as $(\vec{u}_{i+1} - \vec{u}_i)$. Generally speaking, the larger the window size lw, the better chance a snake may have to get around of the undesired local minima. Moreover, a longer searching window would give a better capability of penetrating the energy barriers formed by the noise. A wider searching window would also reduce the possibility of passing by the missing edges for each snaxel. That is, if a breach of the desired boundary is less than w, the snake still has the chance to capture the boundary. However, large l and w imply a longer deformation time, which is not preferable for the clinical use. Empirically, l and w have been set to 9 and 5, respectively, in all implementation results presented in this paper.

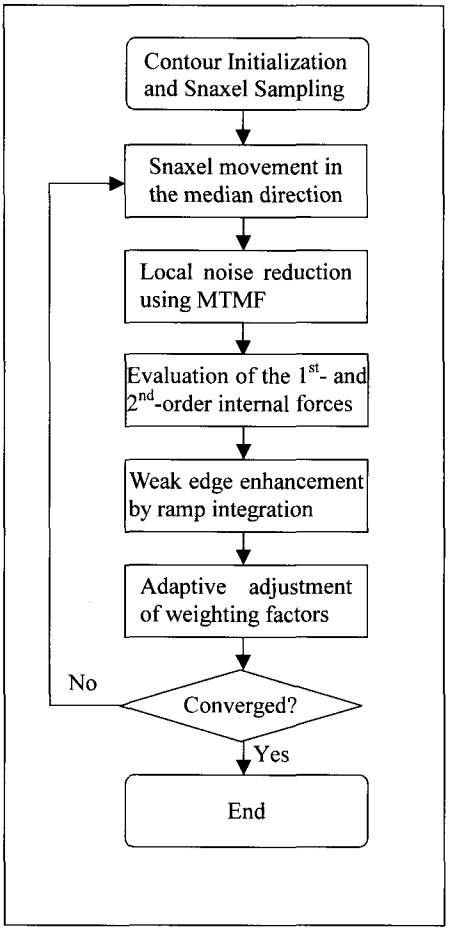

FIG. 1 Block diagram of the proposed snake model.

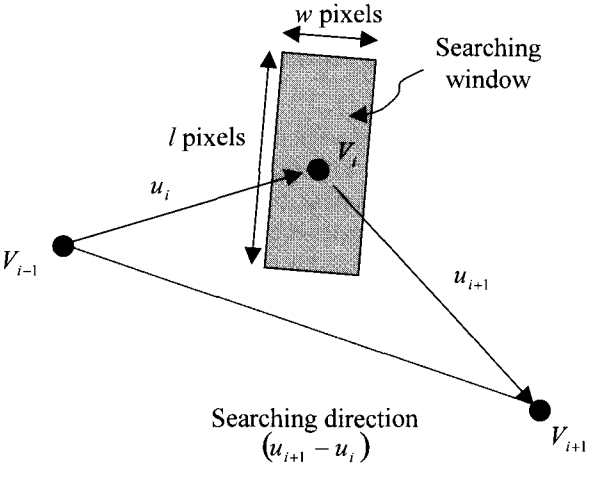

FIG. 2 Searching window for each snaxel to seek for the next position with the lowest energy state to move to. The window is *l* pixels long in the searching direction and *w* pixels wide in the direction perpendicular to the searching direction.

Noise reduction

Noise reduction is an important task in ultrasound image segmentation. Many approaches have been proposed previously to deal with the speckle noise in ultrasound images. For example, Czerwinski et al[20] employed a bank of oriented one-dimensional median filters attempting to suppress speckle noise while retaining the structure of the image. Kotropoulos et al[21] proposed a signal-adaptive maximum likelihood (SAML) filter for ultrasonic speckle removal. Busse et al[22] suggested a geometric filtering method incorporating the models of the transducer geometry, center frequency shifts and beamforming geometry. Nevertheless, because of the complicated noise property, none of the existing speckle reduction schemes has achieved a satisfactory performance. Typical side effects of the speckle reduction operation are over-smoothed edges, lost fine details and artificial edges.

Rather than attempting to solve the hard de-speckle problem, we have aimed to provide a *good* image in a *fast* way for further calculation of the image force. A *good* denoised image would be sufficient for our purpose since the proposed ramp integration technique used to derive the image force has great noise immunity, as demonstrated later. Taking into account the computational time and the performance of denoising, the modified trimmed mean (MTM) filter is adopted for speckle reduction in this study. The MTM filter was proposed by Lee et al[23] in the attempt to combine the advantages of the mean and median filters. Conventionally, the mean filter is known to be effective in dealing with Gaussian-like noise, whereas the median filter is notable for removing shot noise. The MTM filter has shown to be not only an excellent approach to noise reduction and edge preservation for Gaussian noise,[26] but also an effective filter for speckle reduction.[15] The idea of the MTM filter is as follows. Let W_i denote the set of pixels in the window centered at the pixel i of the underlying image for speckle reduction and $w_i(j)$ the value of the jth pixel in W_i. Suppose the number of elements in each window is N. Let m_i represent the median value of all pixel values in W_i. Then, given a threshold t, the output of the MTM filter, denoted as y_i, for the pixel i is defined as

$$y_i = \frac{\sum_{j=1}^{N} a(j) w_i(j)}{\sum_{j=1}^{N} a(j)}$$

where

$$a(j) = \begin{cases} 1, & if \ |w_i(j) - m_i| < t \\ 0, & otherwise \end{cases}$$

Internal forces

As defined in Eq. (1), the energy function of the proposed snake model is composed of the internal force E_{int}, image force E_{image} and external force E_{ext}. The internal force is made up of a first-order force ν_s and second-order force ν_{ss}. These two forces have been employed by many other snake models but with various definitions according to different considerations. In our model, to avoid the aggregation of snaxels during deformation, the first-order force ν_s, which accounts for the length of the snake, is defined as

$$|\nu_s(p_i)|^2 = \left(|\vec{u}_i|^2 + |\vec{u}_{i+1}|^2 \right) / 2 \tag{3}$$

It can be easily shown when $|v_s(p_i)|^2$ is minimized, $V_i = (V_{i-1} + V_{i+1})/2$. That is, minimization of the first-order force v_s tends to shrink the snake and make all snaxels equally spaced.

The second-order force v_{ss} regularizes the smoothness of the snake, which is defined as

$$v_{ss}(p_i) = -\cos^{-1}\left(\frac{\vec{u}_i \cdot \vec{u}_{i+1}}{|\vec{u}_i| \cdot |\vec{u}_{i+1}|}\right) \tag{4}$$

where $0 \le v_{ss} \le \pi$. In other words, the second-order force v_{ss} is the angle formed by the two vectors $\vec{u}_i$ and $\vec{u}_{i+1}$. Minimization of v_{ss} has a tendency to smooth the snake. The maximum curvature that can be captured by the snake depends on the relative strength of the weighting factors of all energy terms.

Image force

While v_s provides the shrinking force and v_{ss} controls the snake smoothness, the image force plays the decisive role in attracting a snake toward the desired boundary. An ideal image force should exert the most significant power at the desired boundary. To characterize different types of boundary, various image forces have been proposed in the past. For examples, the gradient[14] of an edge has been frequently used to represent the strength of a nontextural edge. On the other hand, textural features like distance map[24] have been employed to distinguish the textual edges. Although both textural and nontextural edges exist in an ultrasound image, this paper will emphasize the characterization of nontextural edges. A discussion of the image force exerted by the textural edges in ultrasound images may be found in Chen et al.[24]

The gradient of an edge, though not the only one, is one of the most widely-used image forces to guide snake deformation in a nontextural image. For a step edge, the gradient does offer an outstanding feature at the edge position. However, using the gradient of an edge as the image force suffers at least two fundamental problems in practice. One is that it is very sensitive to the noise. Although a denoising process is usually applied before the gradient is calculated, the gradient of the residual noise may still be significant enough to interfere with snake deformation. The other problem is that the edges in an ultrasound image are mostly ramp rather than step edges due to the artifacts and similar acoustic impedance between two tissues. Moreover, the denoising process may further reduce the slope of the ramp edges. As a result, compared to the internal forces, the gradients of the ramp edges at the desired boundary may not be large enough to capture the snake.

To avoid the potential problems that a gradient type of image force may have, we propose in this paper a new image force called *ramp integration*, denoted as I_Σ, that may amplify the weak edges and further suppress the residual noise at the same time. Instead of using the gradient to characterize an edge, ramp integration quantifies the edge strength by the sum of the regional level variations as defined in the following. Suppose that e_j denotes the gray level of the j^{th} pixel on a line profile along the search direction of a snaxel in the search window. Note that in each search window, there would be w parallel line profiles to be used for computing ramp integration. Then the ramp integration I_Σ of the j^{th} pixel on a line profile is given by

$$I_\Sigma(e_j) = \frac{2}{r}\left\{\left|\sum_{k=j-r+1}^{j}(e_k - e_j)\right| + \left|\sum_{k=j}^{j+r-1}(e_k - e_j)\right|\right\} \tag{5}$$

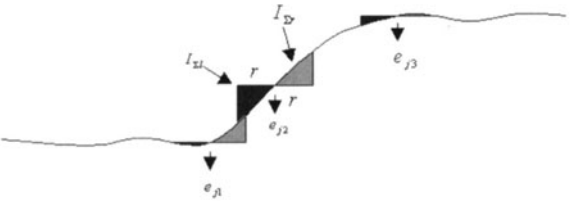

FIG. 3 Illustration of ramp integrations for three different pixels on a ramp edge in which e_{j1} and e_{j3} represent the ramp integrations at both ends of the ramp edge and e_{j2} the ramp integration in the middle part of the ramp edge.

For each e_j, the idea of the ramp integration is to sum up the gray level variations relative to the e_j within a window of radius r. The first and the second summation terms in Eq. (5) account for the overall gray level variations to the left and right of e_j, which are termed *left ramp integration* and *right ramp integration*, respectively. The multiplicative term $2/r$ is the normalization factor. Figure 3 illustrates the ramp integrations for three different pixels on a ramp edge, in which the dark area corresponds to left ramp integration and the light area to right ramp integration. Of these three pixels, e_{j1} and e_{j3} represent the ramp integrations at both ends of the ramp edge, and e_{j2} the ramp integration in the middle part of the ramp edge. From this figure, it is clear that the pixels toward the two ends of a ramp edge, e.g., e_{j1} and e_{j3}, are expected to have a smaller ramp integration than those pixels in the middle part, like e_{j2}. The reason is that at least one of the left and right ramp integrations is relatively small at the two ends of the ramp edge. Therefore, it is reasonable to expect a local maximum in the middle part of a ramp edge rather than at its both ends.

Empirically, we have found that the ramp integration has two advantages over the gradient of an edge. The first one is that compared to the gradient of an edge, the ramp integration tends to make a larger amplification for a wide and slowly- varying edge, and a smaller amplification for a narrow and fast-changing edge. With this feature, the image force formed by the ramp integration is expected to be more capable of capturing the weak edges than the image force given by the gradient. The second advantage is that the ramp integration is more immune to the noise than the gradient. These two advantages will be demonstrated by examples in next section.

Adaptive adjustment of weighting factors

Determination of the weighting factors is a very difficult issue in practical implementation of a snake model. Most existing snake models have adopted constant weighting factors for simplicity. However, in practice, the relative importance of the underlying snake force changes during snake deformation. When the snake is distant from the object of interest, the image force plays the major role in attracting the snake toward the desired boundary. For example, Xu et al[25] has developed the concept of an attracting force, called the gradient vector flow, based on the gradient of the image attempting to guide a distant initial contour toward the desired boundary. Nevertheless, when the snake is quite close to the desired boundary, the internal force, especially the curvature, is expected to polish the smoothness to obtain a smooth contour. Unfortunately, the actual distance between the snake and the desired boundary cannot be formulated correctly during the snake deformation. As a reasonable alternative, we suggest in this paper to adjust the weight of the image force for the i^{th} snaxel, denoted as $\gamma(p_i)$, according to Eq. (6), while keeping the weights of the first-order and second-order internal forces constant, denoted as α and β, respectively.

$$\gamma(p_i)=\begin{cases}\gamma_2 & if\ g_i>\gamma_1\\ \dfrac{\gamma_2}{g_i} & if\ g_i\le\gamma_1\end{cases} \tag{6}$$

where g_i is the gray level of the denoised image of the i^{th} snaxel p_i at each pixel position in the searching window, γ_2 is a constant to balance the internal and image forces and γ_1 is an offset constant to prevent amplifying an insignificant image force. Eq. (6) attempts to approximate the above idea of emphasizing the image force of a distant snaxel by giving a larger weight to a smaller image force. The rationale behind this approximation is that in a searching window, a small image force is more likely to be farther away from the desired boundary than a large image force.

In summary, the proposed snake model starts with a set of equal-interval snaxels on a manually drawn initial contour. At each step, each snaxel moves to the pixel position with the lowest energy state within its own searching window defined in the searching direction. Before the energy at each pixel position is computed, the modified trimmed mean filter is applied to alleviate the noise interference. Since only the energy variation caused by each individual snaxel needs to be considered for its movement, the energy function guiding the snake deformation may be simplified to describe the energy of each snaxel as

$$E_{snake}(p_i)=\min_{\Omega_i}\left\{\alpha\,|\,v_s(p_i)\,|^2+\beta\,|\,v_{ss}(p_i)\,|^2+\gamma(p_i)I_\Sigma(e_j)\right\} \tag{7}$$

where Ω_i is the set of pixels in the searching window of the snaxel p_i at the current step. An optional constraint force may be imposed on the proposed snake model, if necessary. If a polygonal initial contour is made, then some of the vertices may be defined as fixed points, i.e., they remain in the initial positions during snake deformation. The immobility of these fixed points may serve as a constraint force to help the snake move toward the desired boundary. The snake deformation stops when less than m% of snaxels change position in an iteration, where m is set to 2 in this study.

2.2 Images for performance analysis

Two types of images are employed to evaluate the performance of the proposed snake model. One is the phantom image and the other is the clinical ultrasound image. A phantom image is a simulated ultrasound image consisting of an object of interest with a known boundary and simulated speckles. Since the boundary of the object of interest is well defined, the phantom image serves for an exact evaluation of the correctness of the boundary derived by the proposed snake model. On the other hand, the clinical ultrasound image provides a real complex image condition, including the speckle and the tissue-related textures, for performance evaluation of the proposed algorithm. The boundaries obtained by the proposed snake model are compared to those manually drawn by an experienced medical doctor. However, since delineating the boundary of an object of interest manually is quite a subjective process, the delineated boundary may be different for different medical doctors or even for the same medical doctor at different times. Therefore, even though it is valuable to carry out a performance evaluation on the clinical ultrasound images, it is more appropriate to regard the analysis results as a reference.

The ultrasound images used in this study were selected by medical doctors and captured from a Toshiba SSA-380A clinical ultrasound imaging system through a frame grabber card. The image was from the RGB output of the Toshiba SSA-380A and captured by the frame grabber card, Meteor-II card, made by the Matrox Electronic System Ltd. The captured image was stored in BMP format with 8-bit resolution for each color channel. All clinical ultrasound images are liver images and the objects of interest are hepatic tumors. The types of hepatic tumors include hepatocellular carcinoma (HCC), cavernous hemangiomas, metastatic liver cancer, etc. Using one hepatic ultrasound image from each patient, we have chosen 16 hepatic tumors, each from a clinical ultrasound image, for performance evaluation of the proposed snake model. Among these 16 hepatic tumors, 7 of them were hypoechoic and the others are hyperechoic. The boundaries of all 16 tumors were roughly convex.

For the phantom image, the ramp edges have been designed for the object of interest to simulate real edges in an ultrasound image more closely. The phantom image is created as follows. Firstly, a uniform disc phantom of radius 64 is placed at the center of a 256×2 56 uniform image. Let g_f and g_b denote the gray levels of the disc and the rest of area, respectively. For convenience, this phantom image is called the *disc image*. Then, the disc image is blurred by a Gaussian filter of standard deviation σ_g and the resulted image is called the *blurred disc image*. Note that the edge of the disc is a step edge, whereas the edge of the blurred disc is a (Gaussian) ramp edge. Finally, the blurred disc image is corrupted by the speckle, which gives the *ramp phantom image*. The contrast-to-noise ratio (*CNR*) of the ramp phantom images is defined as

$$CNR = \frac{|g_f - g_b|}{\max(\sigma_f, \sigma_b)} \tag{8}$$

where σ_f and σ_b are the standard deviations of the speckle within and outside the blurred disc. Note that the speckles on the ramp edge of the blurred disc are not taken into count in computing σ_f and σ_b.

Given a blurred disc image, the speckle in the ramp phantom image may be simulated in two possible ways. The first one is to directly simulate the speckle in a displayed ultrasound image. The second is to simulate the echo envelope signal first, followed by log-compression to generate the displayed ultrasound image. Because of the log-compression process, the statistical models used by these two approaches are quite different. The speckle is caused by the coherent interference of backscattered echoes from the scatterers smaller than the resolution size. When the effective scatterer density is high, i.e., the effective number of scatterers per resolution cell is larger than 10, the speckle is fully developed and the statistics of the echo envelope is Rayleigh distributed. It is well known that except the mean gray level, the first and second order statistical characteristics of the fully developed speckle are independent of tissue types.[27] When the number of effective scatterer density is smaller than the Rayleigh limit, the speckle is partially developed and the statistics of the echo envelope can be modeled by the *K* distribution.[28,29] For the displayed ultrasound image, the statistics of the fully and the partially developed speckle may be closely modeled by the *K* distribution as shown by Dutt and Greenleaf.[29] They also showed that the density function of the log-compressed fully developed speckle may be modeled by a double exponential or Fisher-Tippett distribution.[29]

Following the speckle simulation algorithm used by Li et al,[30] the fully developed speckle has been simulated in this paper by using the second approach. The speckle is modeled as a random walk in the complex plane. Each step in the random walk stands for the signal re-

ceived by the transducer from a scatterer in the resolution volume. With the assumption of high effective scatter density, each of the real and imaginary parts of the summed signal is modeled by a Gaussian distribution. It follows that the amplitude of the summed signal is Rayleigh distributed.

The scanner is assumed to be a 128-element linear array. The interelement spacing is 0.25 mm. The central frequency is 3 MHz and the bandwidth is 1 MHz. The vertical axis of the simulated image represents the axial direction. For the axial response, the shape of the envelope is assumed to be Gaussian. On the other hand, by assuming a continuous wave model, the lateral response is derived by Fourier transforming the aperture function. For simplicity, it is assumed that the point spread function of the scanner is spatial invariant. Denote the blurred disc image by B. The ramp phantom image, R, is generated as follows.

Step 1. Compute $B_1 = 10^{B/20}$.

This step ensures that after taking log-compression of the simulated echo envelope, the mean values within and outside of the blurred disc, excluding the area covered by the ramp edge, are approximately equal to g_f and g_b, respectively.

Step 2. Generate the summed signal $S_r + iS_i$.

S_r and S_i represent the real and timaginary parts of the summed signal, both of which are Gaussian distributed.

Step 3. Derive the point spread function of the scanner, P.

Step 4. Compute the echo envelope, $E = (B_1(S_r + iS_i)) \otimes P$.

The operator $\otimes$ denotes 2D convolution. That is, the echo envelope is derived by convolving the point spread function with the product of B_1 and the summed signal.

Step 5. Compute the log-compressed echo envelope, $L = 20 \log_{10} \|E\|$.

Step 6. Convert the log-compressed echo envelope, L, into the ramp phantom image, R, by rounding the value of each pixel to the nearest integer and setting all negative pixel values to 0.

Note that steps 1 and 6 have been designed to ensure that all ramp phantom images with various *CNR* used for performance evaluation have the same type of edges, i.e., the edges of all blurred discs corrupted by the speckle are the (Gaussian) ramp edges. It is for the same reason that no attempt has been made to adjust the dynamic range or the image contrast of the ramp phantom images. The dynamic range of the ramp phantom image is basically determined by the specified blurred disc.

3. RESULTS AND DISCUSSION

To demonstrate the performance of the proposed schemes, this section reports the experimental results for the ramp integration and the adaptive snake model on the phantom and real ultrasound images.

Performance of ramp integration

Figure 4 shows a typical response of the ramp integration. In figure 4, the 'Gaussian edge' is made by smoothing an ideal step edge with a Gaussian filter. The edge location of the ideal edge is at pixel 65. The standard deviation of the Gaussian filter employed for this case is 5, which is indicated as std = 5 The ramp integration is computed using a radius $r = 5$. The gradient of the pixel i is the gray level difference of the pixels i-1 and i+1. It is clear that both the ramp integration and gradient give maximum values at pixel 65.

Using the Gaussian edges with various standard deviations but the same height, figures 5 and 6 illustrate the maximum responses of the ramp integration for different radii. All these

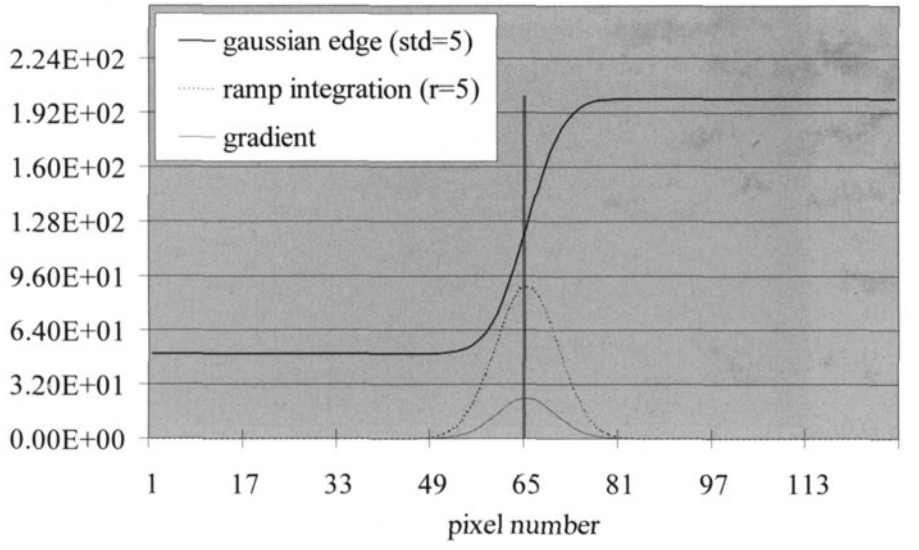

FIG. 4 Typical response of ramp integration and gradient for Gaussian edge.

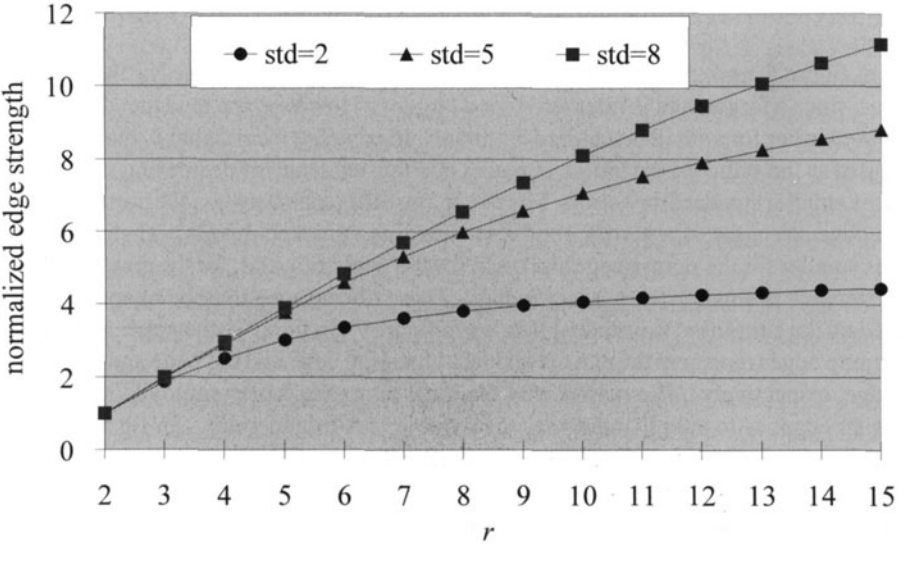

FIG. 5 Normalized maximum edge strengths of the ramp integrations derived by using different radii for three Gaussian edges (ramp edges) with different slopes, including std = 2, std = 5, and std = 8.

maximum responses occur at pixel 65. In figure 5, the maximum edge strengths derived by using different radii, ranging from 2 to 15, are plotted for three Gaussian edges (ramp edges) with different slopes, including std = 2, std = 5 and std = 8. For each of these three curves, the maximum edge strengths are normalized by that of the r =2 case. On the other hand, in figure 6, the maximum edge strengths derived by using different standard deviations, ranging from 1 to 15, are plotted for three radii, including r = 5 r = 8 and r = 11 For each of these three curves, the maximum edge strengths are normalized by that of std=1 case. For com-

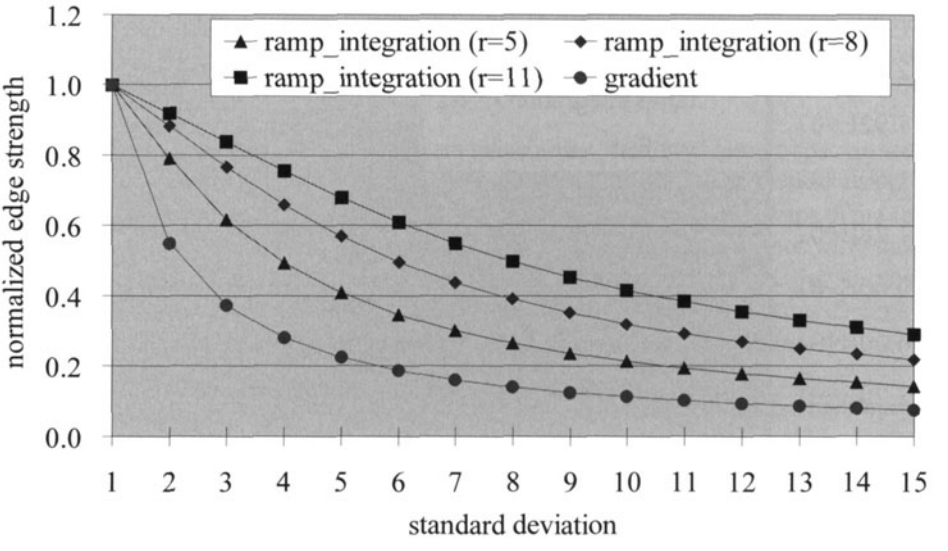

FIG. 6 Normalized maximum edge strengths of the ramp integrations derived using three radii, including $r = 5$, $r=8$ and $r=11$, for the Gaussian edges with different standard deviations.

parison, the normalized maximum edge strength for the gradient approach is also provided in figure 6.

From figure 5, as expected, one can see that the maximum I_Σ increases as the radius r increases, since a larger area is integrated for a larger r. However, the tendency of increasing *saturates* earlier for a smaller standard deviation. In contrast, from figure 6, the maximum I_Σ decreases as the standard deviation increases and this tendency of decreasing *saturates* earlier for a smaller standard deviation. Moreover, the difference between the normalized maximum edge strengths of a narrow- and fast-changing edge and a wide and slowly varying edge is smaller for the ramp integration than for the gradient. And, for the ramp integration, the difference is smaller for a larger radius. These phenomena may be quantitatively explained by the simplified example illustrated in figure 7. In figure 7, the upper and the lower ideal ramp edges represent the narrow and fast-changing edge and the wide and slowly varying edge, respectively. The reason why the ideal ramp edges are employed instead of the Gaussian edges is to simplify the analysis without loss of generality. In figure 4, it is assumed that the width of the upper edge w is smaller than the diameter of the ramp integration window $2r$. For these two ideal ramp edges, one can easily show that the maximum ramp integration and the maximum gradient, which occurs at the center of both edges, are:

(1) Upper ramp edge — maximum gradient: $\tan\theta$; maximum ramp integration: $2w\tan\theta(r\text{-}w/4)/r$

(2) Lower ramp edge — maximum gradient: $\tan\theta$; maximum ramp integration:$2r\tan\theta$

From this formulation, the saturation phenomenon in figure 5 may be explained as follows. Given a ramp edge, consider the radii $r = 2$ to R, where $2R > w$. When the edge width w is larger than the diameter of the ramp integration window $2r$, the normalized maximum ramp integration is $2r\tan\theta/4\tan\theta = r/2$, which is linearly proportional to r. However, when the edge width w is smaller than the diameter of the ramp integration window $2r$, the normalized maximum ramp integration approaches to a constant as r increases, which accounts for the saturation phenomenon.

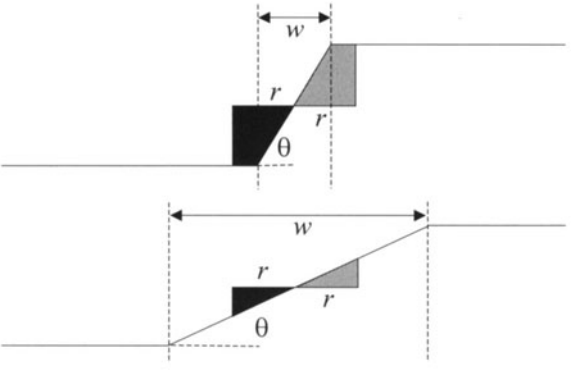

FIG. 7 Upper and lower ideal ramp edges representing the narrow and fast-changing edge and the wide and slowly-varying edge, respectively.

On the other hand, given a radius r, the phenomena observed in figure 6 may be explained using the simplified formulation as follows. Suppose the height of the ramp edge remains constant, denoted as h, as assumed in figure 6. Consider θ monotonically decreasing from θ_0 to θ_n, which are used to approximate the Gaussian edges with the increasing standard deviations. Then, when $w < 2r$, the normalized maximum ramp integration becomes $(r-(h \cot\theta)/2)/(r-(h \cot\theta_0/2)$, which monotonically decreases when θ decreases, as shown in figure 6. When $w \geq 2r$, the normalized maximum ramp integration is $r^2 \tan\theta/[h(r-(h \cot\theta_0/2)]$. Since r, h, and θ_0 are constants for each curve, one may expect a saturated normalized maximum ramp integration for a wide and slowly-varying ramp edge. It is because $\tan\theta$ changes slowly with a small θ. Also, it is clear that a larger r will produce a larger saturation level.

These analyses, based on the ideal ramp edges, may be further verified in figure 8. The edge strengths in figure 8 are derived by varying w and h, but fixing θ. That is, the ramp integration is computed for different scales of ideal ramp edges with the same slope for a given radius. As analyzed above, the ramp integration technique generates the full edge strength only if the edge width is large enough. And the saturation level is higher for a larger ramp integration window.

Although these examples and analyses are only for relatively simple cases, they do provide a general idea that compared to the gradient technique, the ramp integration technique can give a better edge strength for a weak edge, which is wide and slowly-varying. It is accomplished by giving a larger amplification to the weak than to the strong edges. When a weak edge is not wide enough, the ramp integration technique will produce only partial amplification. Implicitly, the ramp integration technique has assumed that a weak edge is significant only if it is wide enough. In contrast, the gradient technique concerns only about the slope of an edge and disregards the width of the edge.

Another important advantage of the ramp integration technique over the gradient technique is better noise immunity, which results from the averaging effect inherent in the integration approach. It smoothes out the small and fast varying noises and de-emphasizes the slight gray level change between two adjacent regions. As an example, figure 9 gives the ramp integration I_Σ using $r = 5$ and the gradient of a Gaussian edge with std = 10 corrupted by a sinusoidal noise. Apparently, the ramp integration has successfully suppressed the small and fast varying noises and given an outstanding peak at pixel 65. On the contrary, the gradient is very sensitive to the fast varying noises even if they are insignificant compared to the edge width and height.

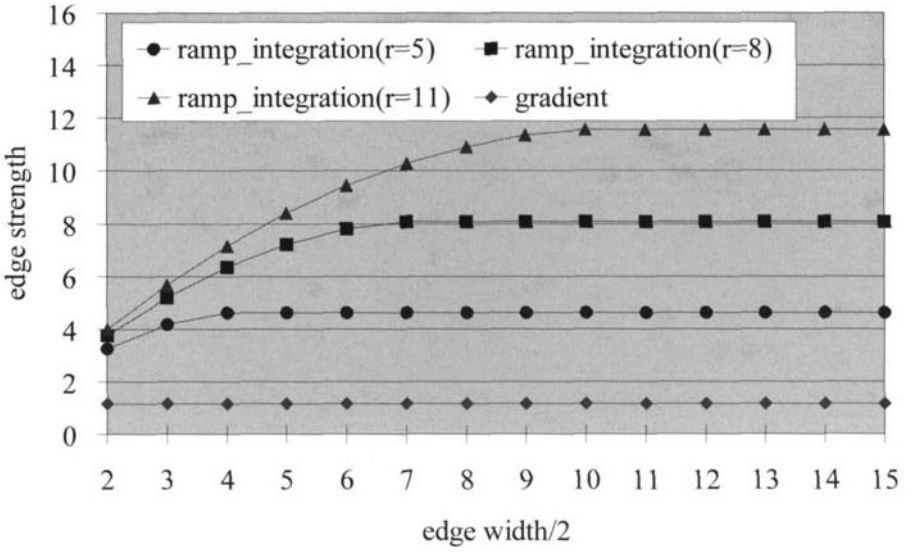

FIG. 8 Edge strengths of ramp integrations derived using different radii for the ideal ramp edges with a constant θ and different w and h as defined in figure 7.

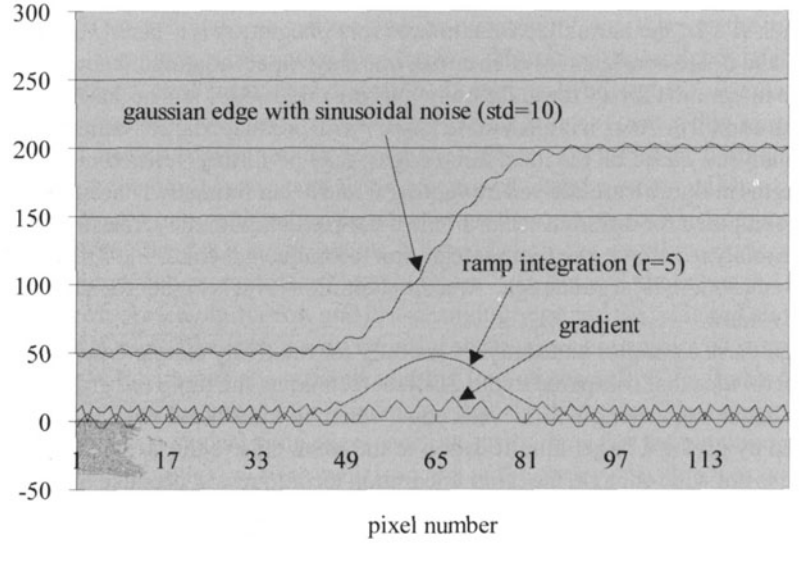

FIG. 9 Ramp integration with r=5 and the gradient of a Gaussian edge with std=10 corrupted by sinusoidal noise.

As another example, figures 10 and 11 illustrate the performance of the ramp integration and the gradient techniques on a denoised ramp phantom image. Figures 10(a) and (b) shows a disc image with $g_f = 120$ and $g_b = 90$, and its corresponding blurred disc image with $\sigma_g = 5$, respectively. Figure 10(c) gives the ramp phantom image with $CNR = 5.25$. Figure 10(d) provides the denoised ramp phantom image using the MTM filter with the threshold t set to σ_b. The profiles of the two white line segments marked in figures 10(c) and (d) are plotted in fig-

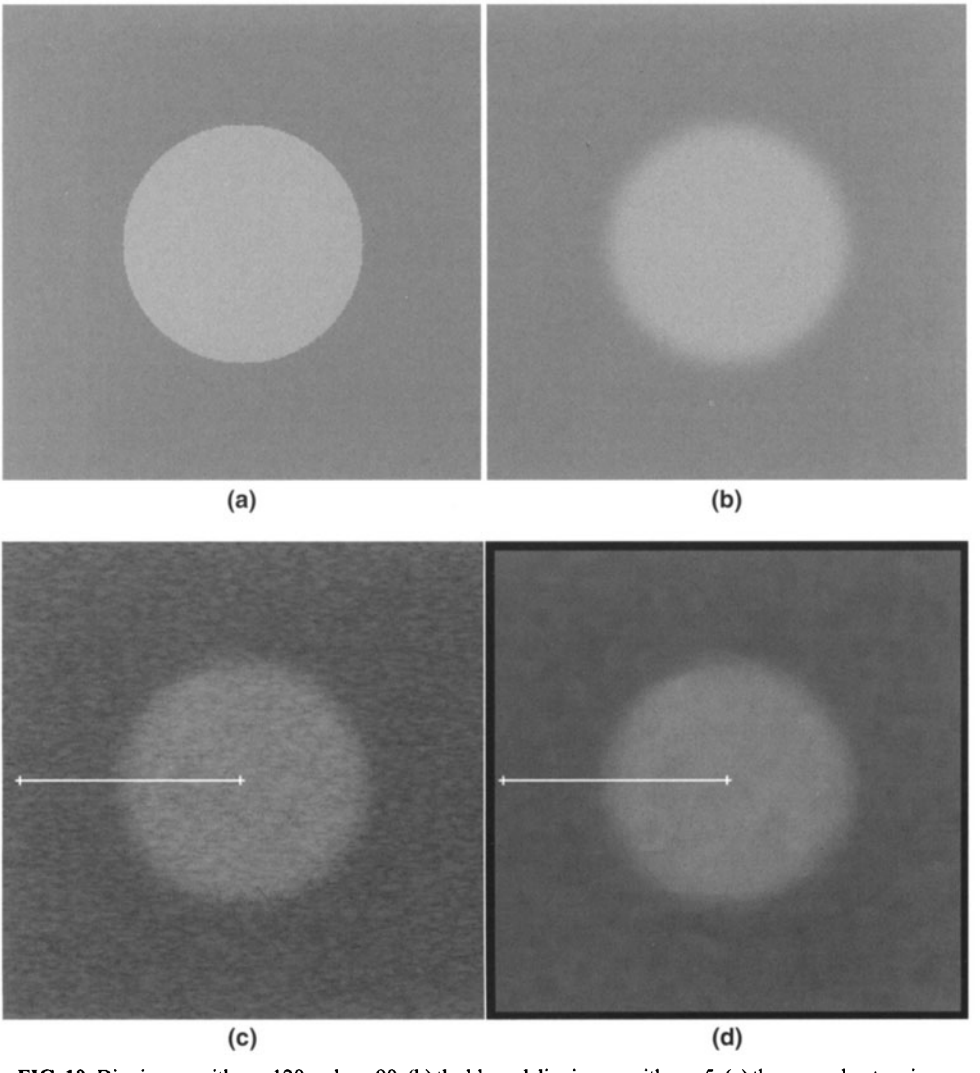

FIG. 10 Disc image with $g_f = 120$ and $g_b = 90$; (b) the blurred disc image with $\sigma_g = 5$; (c) the ramp phantom image with *CNR* = 5.25; and (d) the denoised ramp phantom image using the MTM filter with the threshold t set to σ_b.

ure 11, which are labeled as 'original' and 'mtmf', respectively. The results obtained by applying the ramp integration with $r = 5$ and the gradient technique to the denoised line profile, i.e., 'mtmf', are plotted and labeled as 'ramp integration' and 'gradient' in figure 11, respectively. Note that figure 11 has two vertical axes. The left is for 'original' and 'mtmf' and the right for 'ramp integration' and 'gradient.' The desired boundary location is at pixel 65 and is marked by the double vertical dashed line. It is obvious that the ramp integration technique is better than the gradient technique in the sense that the former has a more significant peak at the desired location, i.e., pixel 65, than the latter. In this case, the ratios of the maximum to the second maximum are 1.95 and 1.25 for the 'ramp integration' and 'gradient,' respectively.

Performance of proposed snake model

The proposed snake model has been applied to both phantom and clinical ultrasound images for performance evaluation. To examine the effect of the *CNR* on the performance of

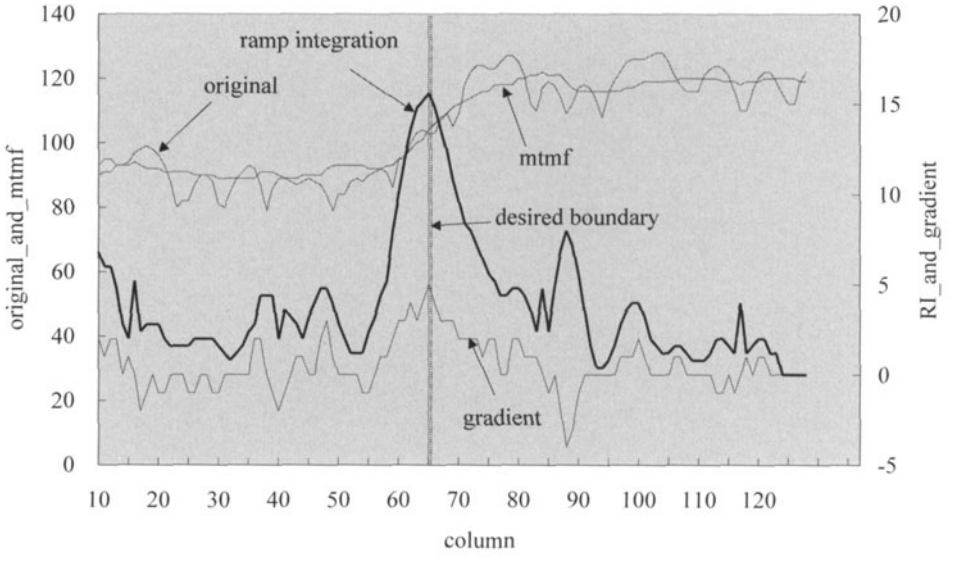

FIG. 11 Ramp integration and gradient for denoised Gaussian edge. The maximum edge strength of the ramp integration is much more significant than that of the gradient.

the proposed snake model, 10 ramp phantom images with various *CNR's* have been employed. Figure 12 illustrates the performance of the proposed snake model on the ramp phantom images with the *CNR* = (0.5, 1-9). All 10 ramp phantom images were created using the same $\sigma_g = 5$. The g_f and g_b have been selected according to the given *CNR* and the standard deviation of the generated speckle. Note that all 10 ramp phantom images have different speckles generated from different random number sequences. The initial contour has been placed 15 pixels away from the actual boundary for all tested cases. The radius of the ramp integration is 5.

In figure 12, 'Mean' represents the mean minimal distance from each derived boundary point to the actual boundary, 'Std' denotes the standard deviation of the minimal distances from the derived boundary points to the actual boundary and 'Max' stands for the maximum of the minimal distance from each derived boundary point to the actual boundary. For the visual inspection, figures 13(a)-(d) give the initial contours and derived boundaries for the cases of *CNR* = 0.5, 2, 4, 6, respectively. The object of interest, i.e., the blurred disc in figure 13(a) is hardly visible because of the very low *CNR*, which is equal to 0.5. As the *CNR* increases, the blurred disc becomes more apparent and the speckle less significant. From figure 12, the performance of the proposed snake model clearly depends on the *CNR* of the object of interest. Generally speaking, the performance degrades as the *CNR* decreases. When the *CNR* is as small as 0.5, 'Max' may be as large as 8.6 pixels. However, figure 12 shows that the minimal distances from most derived boundary points to the actual boundary are within 3.3 pixels (i.e., 'Max+Std' for $CNR \geq 1$). And, the mean minimal distances for those cases with can be as small as 1.7 pixels.

For the clinical ultrasound images, the proposed snake model has been applied to segmentation of 16 hepatic tumors, each from a liver ultrasound image. The initial contours have been placed about 10 to 20 pixels away from the desired boundaries. As examples, figures 14-17 demonstrate the segmentation results for four of the 16 tested ultrasound images, which are images 1, 3, 6 and 12. Two of them (images 3 and 12) contain hypoechoic tumors and the other two (images 1 and 6) contain hyperechoic tumors. For each of these four fig-

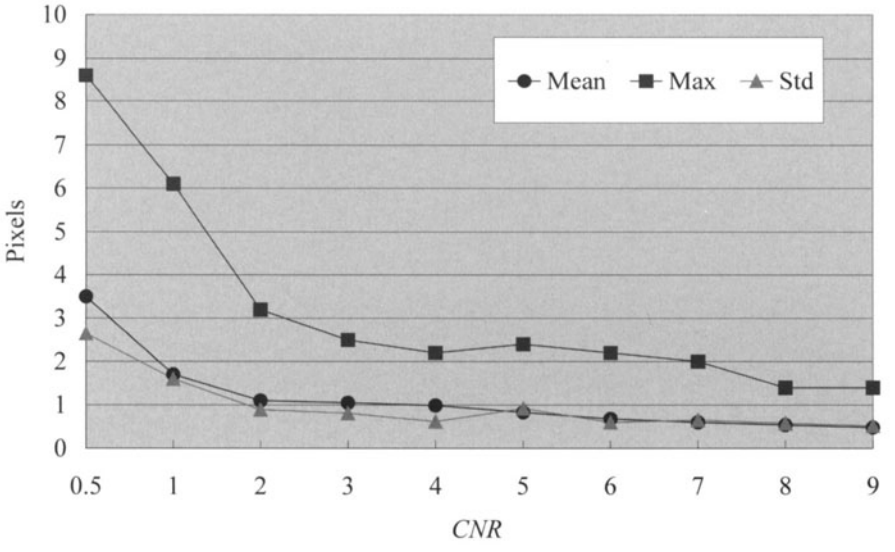

FIG. 12 Performance of proposed snake model on ramp phantom images with *CNR* = (0.5, 1-9).

ures, the first image, which is labeled as (a), is a clip of the original image. The second image, which is labeled as (b), shows the tumor boundary drawn by a medical doctor. The third image, which is labeled as (c), gives the initial contour and the boundary derived by the proposed snake model. Figure 18 plots the performance of the proposed snake model on the 16 tested ultrasound images. The labels for the three curves in figure 18 are defined similarly as those in figure 12. The only difference is that in figure 18, the minimal distance is calculated relative to the manually-drawn boundary rather than to the actual boundary as in figure 12.

Figure 18 shows that compared to the boundary definitions given by the medical doctor, the proposed snake model has attained reasonable boundaries for all tested ultrasound images. For the 16 tested ultrasound images, the 'Mean', 'Std' and 'Max' of the minimal distances are less than 2.5, 1.7 and 5.4 pixels, respectively, for all derived boundaries. The means and the standard deviations of the three curves illustrated in figure 18 are summarized in table 1.

The discrepancies between the derived and manually-drawn boundaries may be ascribed to two major types of sources. The first type of sources is the intrinsic disagreement on the definition of tumor boundaries between different judgements. One possible disagreement results from the different definitions adopted by the image processing approaches and human observation. The image processing approaches usually define an edge based on a certain mathematical model, e.g., the maximum gradient, whereas medical doctors may incorporate their knowledge of medicine and biology in determining the desired edges. An-

TABLE 1. Mean and standard deviation of the 'Mean', 'Std' and 'Max' for the 16 tested ultrasound images (unit: pixels).

	Mean	**Std**	**Max**
Mean	1.56125	1.121875	3.7075
Standard deviation	0.541736	0.33431	1.159158

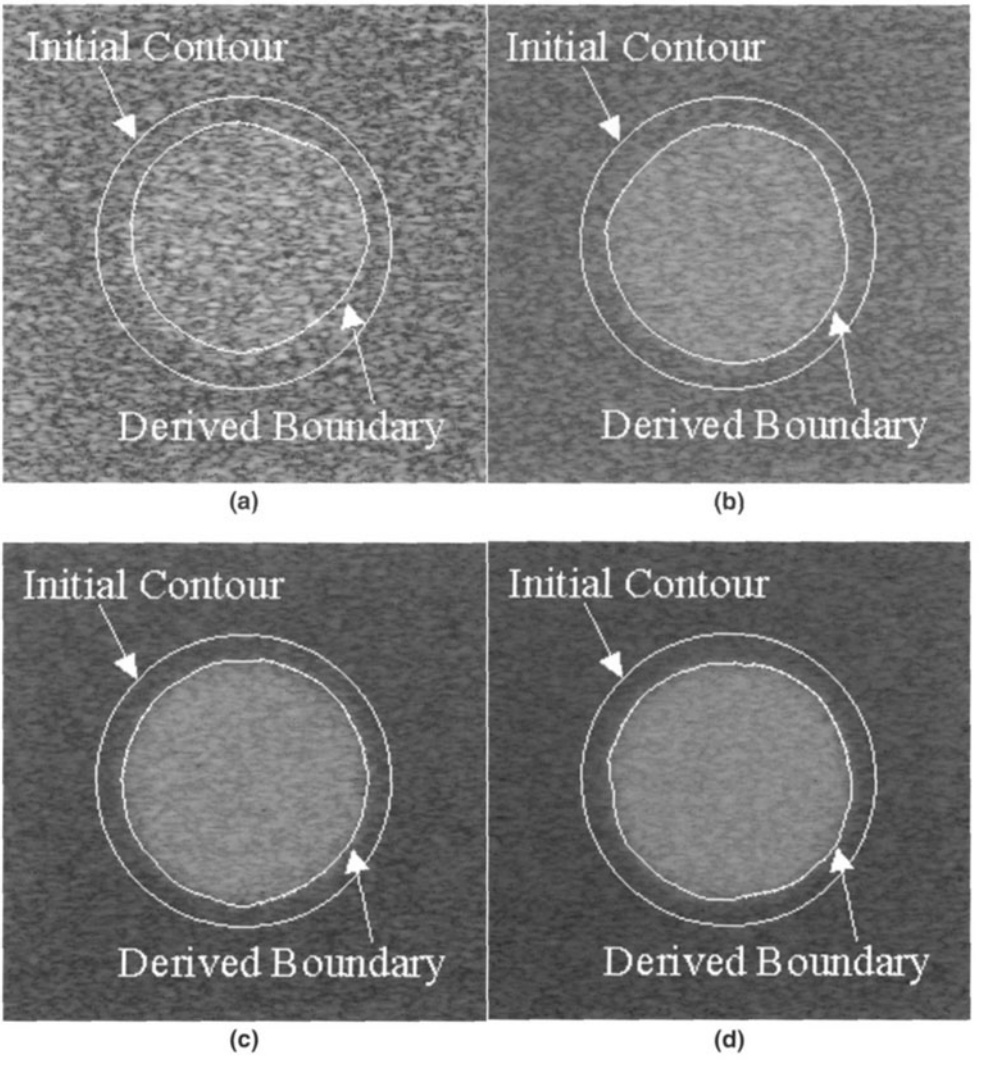

FIG. 13 Boundaries derived by proposed snake model on phantom images with (a) *CNR*=0.5; (b) *CNR*=2; (c) *CNR*=4; (d) *CNR*=6.

other common disagreement generally exists among different human observations, which includes different definitions of tumor boundaries given by different medical doctors and those given by the same medical doctor at different times.

The second type of sources is the complex image property mainly due to the speckles, the weak edges and the sporadic tissue-related textures. The speckles usually take the most responsibility for the noise effect interfering with the detection of the desired boundaries. As simulated in the phantom study, the sole speckle factor may easily cause a mean error greater than one pixel even with a $CNR = 2$. For instance, figure 14 represents the typical case where speckles are the primary source of interference.

The weak edge problem not only makes most snake models fail to converge at the desired boundary, but also increases the difficulty for human observers in determining the actual tumor boundary. Although ramp integration has successfully enabled the proposed snake model to capture the weak edges, when the edges are so weak that they are hardly visible, it

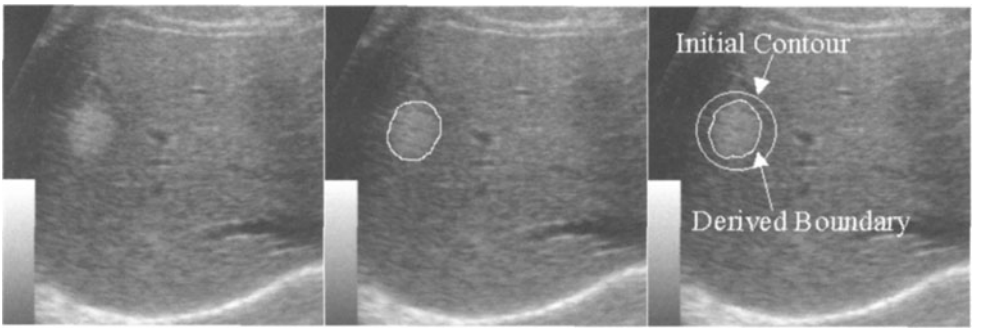

FIG. 14 Segmentation result of testing of ultrasound image 1: (a) clip of original image; (b) manually-drawn boundary; and (c) initial contour and boundary derived by proposed snake model.

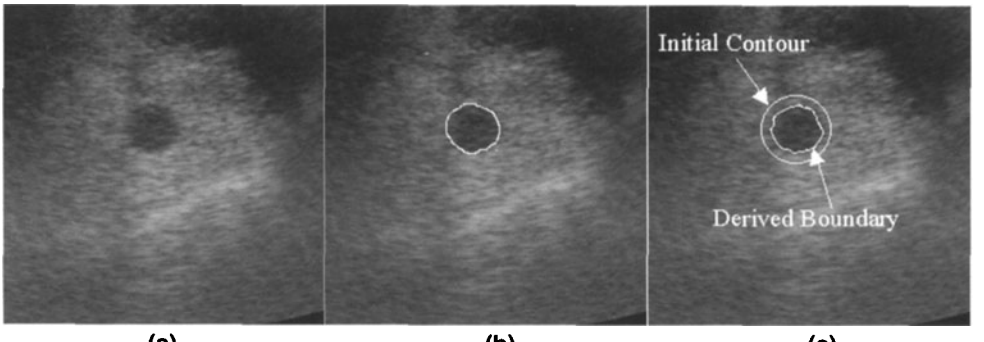

FIG. 15 Segmentation result of testing of ultrasound image 3: (a) clip of original image; (b) manually-drawn boundary; and (c) initial contour and boundary derived by proposed snake model.

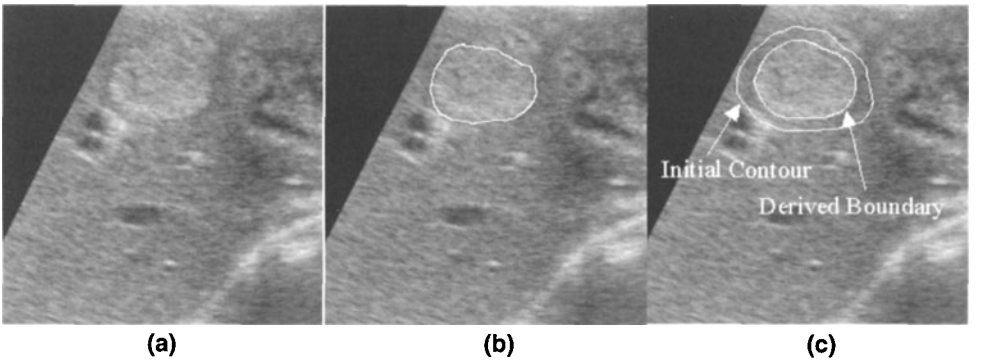

FIG. 16 Segmentation result of testing of ultrasound image 6: (a) clip of original image; (b) manually-drawn boundary; and (c) initial contour and boundary derived by proposed snake model.

may lead to a substantial discrepancies between the manually-drawn boundary and the boundary derived by any image processing approach. As an example, figure 17 illustrates a tumor with weak edges (e.g., the edge at the lower-left portion), where it is difficult to determine the tumor boundary visually.

In addition to the speckles, the sporadic tissue-related textures sometimes act like obstacles to snake deformation, e.g., the tissue-related textures surrounding the tumors in figure 16. Because of these obstacles, the initial contours need to be carefully placed. However, the

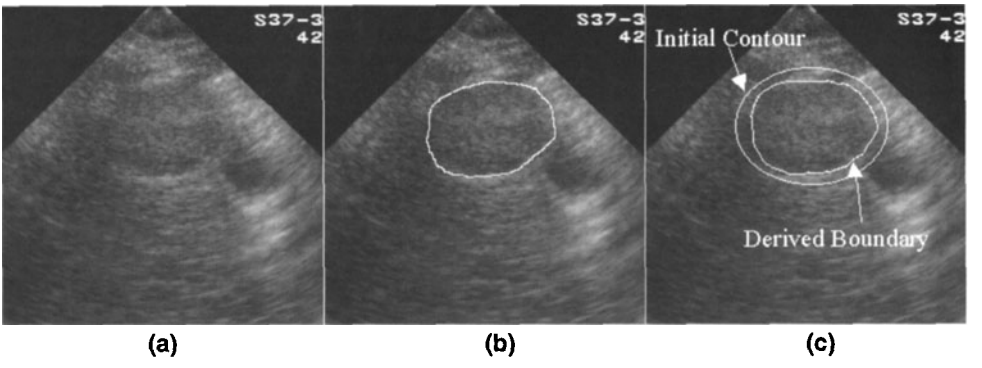

FIG. 17 Segmentation result of testing of ultrasound image 12: (a) clip of original image; (b) manually-drawn boundary; and (c) initial contour and boundary derived by proposed snake model.

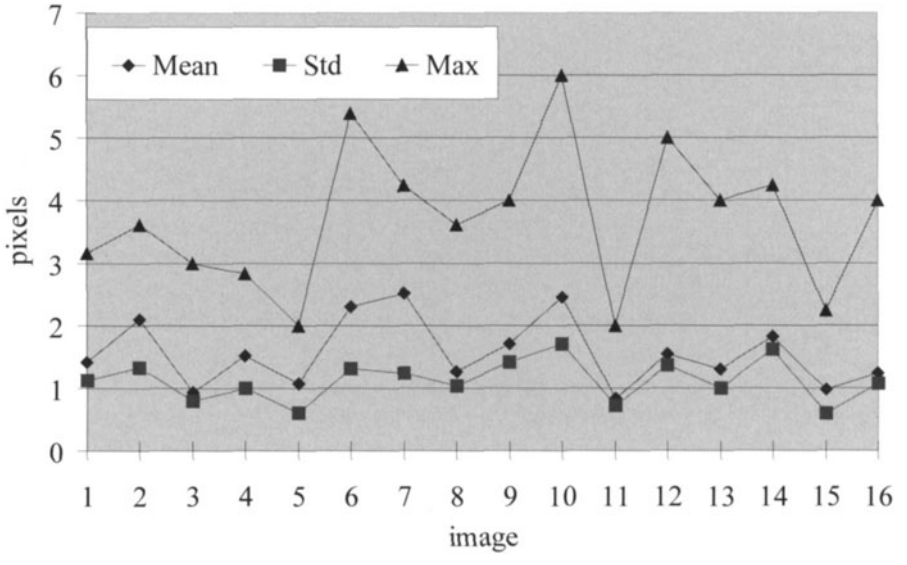

FIG. 18 Performance of proposed snake model on the 16 tested ultrasound images.

snake deformation may inevitably be affected by these tissue-related textures if they are very close to the tumor. For example, the boundary derived by the proposed snake model in figure 16 has been trapped at the undesirable local minimum caused by the tissue-related texture at the upper-right portion of the desired boundary.

4. CONCLUSIONS

Ultrasound image segmentation has been recognized as an important but difficult task for clinical applications. Although the snake model has been widely used in general ultrasound image segmentation, the complex nature of the ultrasound image, such as the speckles, weak edges and tissue-related textures, have seriously degraded the performance of conventional snake models. To cope with this complex image property, a new adaptive snake model has been proposed in this paper for ultrasound image segmentation using three major techniques.

The MTM filter, which possesses the advantages of the mean and median filters, is used to alleviate the interference of the speckles. To capture the weak edges, which may be easily missed by conventional snake models, a new image force, called ramp integration, has been developed. Compared to the gradient technique, the ramp integration technique not only highlights the weak edges, but also provides a better noise immunity for the snake deformation. In the attempt to optimize the role of each energy term, a new scheme is suggested to change the weighting coefficients adaptively at each deformation step. The proposed snake model has been evaluated on phantom and ultrasound images. The experiments on phantom images served for *exact* evaluation since the actual boundaries of the phantom images are known. On the other hand, the boundaries of the objects of interest on 16 tested ultrasound images were defined by an experienced medical doctor as the basis of performance evaluation. The experimental results showed that the proposed snake model has achieved a reasonable performance with an initial contour placed 10 to 20 pixels away from the desired boundary. The mean minimal distances from the derived boundary to the desired boundary have been shown to be less than 3.5 (for $CNR \geq 5$) and 2.5 pixels, respectively, for the phantom and ultrasound images.

REFERENCES

1. Yang, P. M., Huang, G. T., Lin, J. T., Sheu, J. C., et al, Ultrasonography in the diagnosis of benign diffuse parenchymal liver diseases: a prospective study, *J. Formosan Med. Assoc., 87,* 966-977 (1988).

2. Thomas, J.G., Peters, R.A. and Jeanty, P., Automatic segmentation of ultrasound images using morphological operators, *IEEE Trans. Med. Imaging 10*, 180-186 (1991).

3. Heckman, T., Searching for contours, in *Proc. SPIE* 2666, pp. 223-232 (1996).

4. Fan, L., Braden, G. A. and Herrington, D. M., Nonlinear wavelet filter for intracoronary ultrasound images, in *Proc.1996 23rd Ann. Meeting Comp. Cardiol,* pp. 41-44 (1996).

5. Brathwaite, P. A., Chandran, K. B., McPherson, D. D. and Dove, E. L., Lumen detection in human IVUS images using region-growing, in *Proc.1996 23rd Ann. Meeting Comp. Cardiol,* pp. 37-40 (1996).

6. Zimmer, Y., Tepper, R. and Akselrod, S., Two-dimensional extension of minimum cross entropy thresholding for segmentation of ultrasound images, *Ultrasound Med. Biol. 22*, 1183-1190 (1996).

7. Chen, C. H., Lee, J. Y., Yang, W. H., Chang, C. M. and Sun, Y. N., Segmentation and reconstruction of prostate transrectal ultrasound images, *Biomed. Engin. Applications Basis, Commun. 8,* 287-292 (1996).

8. Duquenoy, E., Taleb-Ahmed, A., Reboul, S., Beral, Y. and Dubus, J. P., Modelization of fetal cranial contour from ultrasound axial slices, in *Proc. SPIE, 2588*, pp. 528-537 (1995).

9. Pipelier, F., Solaiman, B., Grassin, S. and Roux, C., New dynamic contour model: Application on ultrasound images, in *Proc. 1996 18th Ann. Int. Conf. IEEE EMBS*, pp. 905-906 (1996).

10. Chalana, V., Linker, D. T., Haynor, D. R. and Kim, Y., A multiple active contour model for cardiac boundary detection on echocardiographic sequences, *IEEE Trans. Med. Imag. 15*, 290-298 (1996).

11. Pathak, S. D., Chalana, V. and Kim, Y. Interactive automatic fetal head measurements from ultrasound images using multimedia computer technology, *Ultrasound Med. Biol. 23*, 665-673 (1997).

12. Tong, A. W. K., Qureshi, R., Li, X. and Sather, A. P., System for ultrasound image segmentation for loin eye measurements in swine, *Canadian Agric. Engin. 40, 47*-53 (1998).

13. Lefebvre, F., Berger, G. and Laugier, P., Automatic detection of the boundary of the calcaneous from ultrasound parametric images using an active contour model; clinical assessment, *IEEE Trans. Med. Imagl. 7*, 45-52 (1998).

14. Kass, M., Witkin, A. and Terzoulos, D., Snake: actour contour models, *Int. J. Comput. Vision 1*, 321-331 (1987).

15. Loupas, T., McDicken, W. N., Allan, P.L., An adaptive weighted median filter for speckle suppression in medical ultrasonic images, *IEEE Trans. Circuits Systems 36*, 129-135 (1989).

16. Vuwong, V. and Yu, H., Shape-based active contour model, in *Proc. SPIE 2898*, pp. 317-326 (1996).

17. William, D. J., A fast algorithm for active contours and curvature estimation, *CVGIP 55*, 14-26 (1992).

18. Saadah, A. K., Galatsanos, N. P. and Bless, D., Motion analysis of videostroboscopic images of the larynx, in *Proc. SPIE 2709*, pp. 156-167 (1996).

19. Huang, C. L. and Chen, C. W., Human facial feature extraction for face intepretation and recognition, *Pattern Recognition 25*, 1435-1444 (1992).

20. Czerwinski, R. N., Jones, D. L. and O rien, W. D. Jr., Ultrasound speckle reduction by directional median filtering, in *Proc. 1995 IEEE Int. Conf. Image Proc.*, pp. 358-361 (1995).

21. Kotropoulos, C., Magnisalis, X., Pitas, I. and Strintzis, M. G., Nonlinear ultrasound image processing based on signal-adaptive filters and self-organizing neural network, *IEEE Trans. Image Proc. 3*, 65-77 (1994).

22. Busse, L. J., Crimmins, T. R. and Fienup, J. R., Model based approach to improve the performance of the geometric filtering speckle reduction algorithm, in *Proc. 1995 IEEE Ultrasonics Symp. 2*, pp. 1353-1356 (1995).

23. Lee, Y. H. and Kassman, S. A., Generalized median filtering and related nonlinear filtering techniques, *IEEE Trans. Acoust. Speech Signal Proc. 33*, 672-683 (1985).

24. Chen, C. M., Lu, H. H.-S. and Lin, Y. C., A new ultrasound image segmentation algorithm based on an early vision model and discrete snake model, in *Proc. SPIE Int. Symp. Med. Imag*, pp. 959-970 (1998).

25. Xu, C. and Prince, J. L., Snakes, shapes, and gradient vector flow, *IEEE Trans. Image Proc. 7*, 359-369 (1998).

26. Fong, Y.-S., Pomalaza-Raez, C. A., Wang, X.-H., Comparison study of nonlinear filters in image processing applications, *Opt. Engin. 28*, 749-759 (1989).

27. Thijssen, J. M. and Oosterveld, B. J., Texture in tissue echogram: speckle or information? *J. Ultrasound Med.* 9, 215-229 (1990).

28. Jakeman, E. and Tough, R. J. A., Generalized *K* distribution: a statistical model for weak scattering, *J. Opt. Soc. Amer. 4*, 1764-1772 (1987).

29. Dutt, V. and Greenleaf J. F., Statistics of the log-compressed echo envelope, *J. Acoust. Soc. Am. 99*, 3817-3825 (1996).

30. Li, P.-C. and O'D onnell, M., Improved detectability with blocked element compensation, *Ultrasonic Imaging 16*, 1-18 (1994).